Postseismic deformation following the June 2000 earthquake sequence in the south Iceland seismic zone

Thóra Árnadóttir,[1] Sigurjón Jónsson,[2] Fred F. Pollitz,[3] Weiping Jiang,[1,4] and Kurt L. Feigl[5]

Received 18 February 2005; revised 23 August 2005; accepted 12 October 2005; published 30 December 2005.

[1] We observe postseismic deformation on two spatiotemporal scales following M_w = 6.5 earthquakes in the south Iceland seismic zone on 17 and 21 June 2000. We see a rapidly decaying deformation transient lasting no more than 2 months and extending about 5 km away from the two main shock ruptures. This local, month-scale transient is captured by several radar interferograms and is also observed at a few campaign GPS sites located near the faults. A slower transient with a characteristic timescale of about a year is detected only by GPS measurements. The month-scale deformation pattern has been explained by poroelastic rebound due to postearthquake pore pressure changes. In contrast, the year-scale deformation can be explained by either afterslip at 8–14 km depth or viscoelastic relaxation of the lower crust and upper mantle in response to the coseismic stress changes. The optimal viscoelastic models have lower crustal viscosities of $0.5–1 \times 10^{19}$ Pa s and upper mantle viscosity of $\sim 3 \times 10^{18}$ Pa s. Because of the limitations of our GPS campaign data, we consider both afterslip and viscoelastic relaxation as plausible mechanisms explaining the deformation field. Both types of postseismic deformation models suggest that the areas of large coseismic stress increase east of the 17 June and west of the 21 June ruptures continue to be loaded by the postseismic deformation.

Citation: Árnadóttir, T., S. Jónsson, F. F. Pollitz, W. Jiang, and K. L. Feigl (2005), Postseismic deformation following the June 2000 earthquake sequence in the south Iceland seismic zone, *J. Geophys. Res.*, *110*, B12308, doi:10.1029/2005JB003701.

1. Introduction

[2] The plate spreading across south Iceland is accommodated by rifting in the eastern volcanic zone (EVZ), and to a lesser extent the western volcanic zone (WVZ), and left-lateral E-W transform motion across the south Iceland seismic zone (SISZ), that connects the two volcanic zones (Figure 1). The relative plate motion across the SISZ is accommodated by right-lateral strike-slip motion on many parallel N-S oriented faults, rather than a single E-W transform fault [*Einarsson and Eiríksson*, 1982; *Einarsson et al.*, 1981]. Sequences of large earthquakes ($M_S \geq 6$) lasting over a time period of days to years have occurred in the SISZ in historical time in Iceland (last 1100 years). Typically, they start with an earthquake in the eastern part of the SISZ and continue with events of equal or smaller magnitude farther west. The time interval between large earthquake sequences in the SISZ ranges between 45 and 112 years [*Einarsson et al.*, 1981], with the most recent one in June 2000. Large localized events have also occurred in the eastern and western ends of the SISZ. Before June 2000, the only instrumentally recorded large earthquake in the SISZ was a M_S = 7.0 in 1912 [*Bjarnason et al.*, 1993a], located in the eastern part of the zone.

[3] The June 2000 sequence started with a magnitude M_w = 6.5 earthquake on 17 June 2000 [*Dziewonski et al.*, 2001; *Stefánsson et al.*, 2003]. Seismicity increased over a large area in SW Iceland following the 17 June main shock, with three M $\geq$ 5 events triggered on Reykjanes Peninsula [*Pagli et al.*, 2003; *Clifton et al.*, 2003; *Árnadóttir et al.*, 2004] (Figure 1). A second large magnitude (M_w = 6.5) event occurred on 21 June 2000 [*Dziewonski et al.*, 2001; *Stefánsson et al.*, 2003], located about 17 km west of the 17 June rupture (Figure 1). Signals from the earthquakes were detected by several local networks: the south Iceland Lowland (SIL) digital seismometers, strong motion accelerometers, volumetric strain meters, and continuous GPS. The earthquakes also caused significant pressure changes in geothermal reservoirs over an extensive area [*Björnsson et al.*, 2001] with local changes correlating well with the focal mechanisms of the two largest events. Surface faulting was observed for the events in the SISZ and on Reykjanes Peninsula, indicating rupture on N-S trending faults [*Clifton et al.*, 2003; *Clifton and Einarsson*, 2005]. The coseismic crustal deformation caused by the two earthquakes was measured with both campaign GPS [*Árnadóttir et al.*, 2001] and interferometric synthetic aperture radar (InSAR) [*Pedersen et al.*, 2001]. These studies used the coseismic geodetic data to estimate fault geometries assuming uniform

[1]Nordic Volcanological Center, Institute of Earth Sciences, Reykjavík, Iceland.
[2]Institute of Geophysics, ETH-Zurich, Zurich, Switzerland.
[3]U.S. Geological Survey, Menlo Park, California, USA.
[4]Now at GPS Research Center, Wuhan University, Wuhan, China.
[5]Centre National de la Recherche Scientifique, Toulouse, France.

0148-0227/05/2005JB003701$09.00

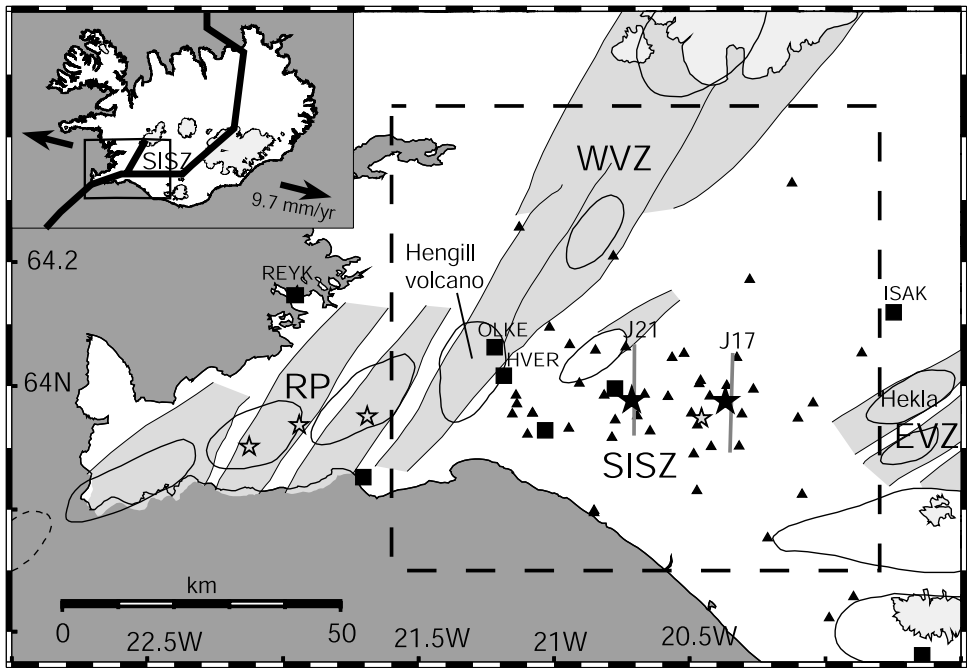

Figure 1. Map of the main tectonic features of southwest Iceland. The epicenters of the 17 and 21 June 2000 earthquakes are shown with large black stars and the four largest aftershocks on 17 June are noted with small gray stars. The locations of the 17 and 21 June fault models are marked by bold gray lines. The locations of the south Iceland seismic zone (SISZ), western volcanic zone (WVZ), and the eastern volcanic zone (EVZ) are also shown. Light shaded areas are individual spreading segments with associated central volcanoes. The dashed box outlines the study area. The locations of the campaign GPS stations are denoted with black triangles, while the continuous GPS stations are shown with black squares. The inset shows the plate boundary across Iceland and the NUVEL-1A plate motion. The location of Figure 1 is indicated by a box.

or simple slip models. A subsequent study combined the InSAR and GPS data to estimate the optimal fault geometries and distributed slip models for the two main shocks [*Pedersen et al.*, 2003].

[4] The June 2000 earthquake sequence provides the first opportunity to study postseismic deformation in Iceland. In this study we concentrate on the long-term postseismic deformation field observed by annual GPS campaigns from 2000 to 2004. To isolate postseismic signals in the observed velocity fields, we correct for the effect of plate spreading, using an interseismic velocity field estimated from preseismic GPS observations. The first months of postseismic deformation contain signals due to postseismic groundwater movements inferred from InSAR measurements [*Jónsson et al.*, 2003]. We use the poroelastic relaxation model from *Jónsson et al.* [2003] to correct the 2000–2001 GPS velocity field. The resulting GPS velocities are then compared to model predictions from bulk viscoelastic relaxation in the lower crust and upper mantle and from afterslip on discrete rupture surfaces below the coseismic ruptures. The signal in the vertical GPS velocity field is marginally larger than the measurement uncertainty and therefore cannot discriminate between afterslip and viscoelastic models.

2. GPS Measurements and Data Analysis

[5] The GPS network in the south Iceland seismic zone has been remeasured every year following the June 2000 earthquakes (Figure 1). The 2000 survey was carried out between 19 June and 3 July when a total of 39 stations were observed, and each site was occupied for at least three 8 hour sessions. Seven stations were observed before the 21 June earthquake, and repeated after the event. In the later surveys, each site was occupied for 2–4 days, with at least one 24-hour session and two sessions of less than 24 hours. All the surveys were performed using dual-frequency GPS receivers, collecting data every 15 s. The next two surveys took place on 20 June to 19 July 2001 (43 stations) and on 2 to 28 October 2002 (44 stations). The 2003 survey was carried out in two parts. The western part of the network was surveyed from 25 June to 2 July, and the eastern part (with six stations reoccupied from the June survey) during 14–27 September (54 stations in total). The survey in 2004 included 41 stations and took place from 3 to 14 May.

[6] We have analyzed all campaign and continuous GPS data collected in the SISZ from 1992–2004 using the GAMIT/GLOBK software [*King and Bock*, 2003; *Herring*, 2003]. The analysis produces three-component time series of daily station positions with respect to the ITRF2000 reference frame [*Altamimi et al.*, 2002]. A second solution describes the station motions in terms of absolute velocities and displacements. The velocities represent the average velocity, equivalent to the slope of the position time series estimated from the GPS observations. The details of the analysis will be discussed in a separate study (T. Árnadóttir et al., Kinematic models of plate boundary deformation in

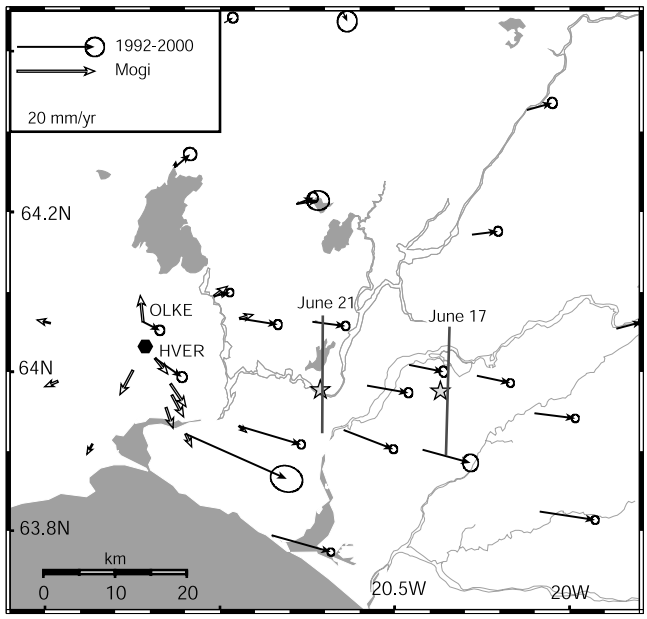

Figure 2. Interseismic plate velocities (black arrows with 68% confidence ellipses), relative to REYK (see Figure 1), calculated from GPS campaign observations from 1992 to 1999. Velocities of two CGPS stations (HVER and OLKE) were obtained from data spanning early 1999 to June 2000. High velocities in the vicinity of the Hengill volcano are due to an inflation episode from 1993 to 1998. The white arrows show velocities predicted by a point source model of inflation at Hengill (shown with hexagon) from 1993 to 1998 [*Feigl et al.*, 2000].

southwest Iceland derived from GPS observations, submitted to *Journal of Geophysical Research*, 2005, hereinafter referred to as Árnadóttir et al., submitted manuscript, 2005). We estimate station velocities for the preseismic time interval (1992–2000), several yearlong postseismic intervals, and a longer interval from June 2001 through May 2004. The GPS station velocities for the time intervals 1992–2000, 2000–2001 and 2001–2004 are given in Tables S1–S3 (auxiliary material[1]). Although the formal uncertainties given here have not been scaled by any a posteriori estimate of variance, previous studies using the same approach indicate that they adequately reflect the data scatter [e.g., *McClusky et al.*, 2000].

3. Interseismic GPS Velocity Field in the SISZ

[7] We estimate a surface velocity field in SW Iceland, representing the background secular motion in the area, using GPS campaign observations from 1992 to 1999 (Figure 2) [*Sigmundsson et al.*, 1995; Árnadóttir et al., submitted manuscript, 2005]. Unfortunately, this velocity field is perturbed in the area around Hengill volcano due to an inflation during 1993–1998 [*Sigmundsson et al.*, 1997; *Feigl et al.*, 2000]. Two continuous GPS stations, HVER and OLKE, were installed in the Hengill area in early 1999. These stations show slower velocities, calculated from data spanning 1999–2000, than the campaign stations 5 to 10 km farther east. This indicates that the inflation period at Hengill ended sometime between late 1998 and early 1999. A model assuming a point source of inflation at ~7 km depth, fitting a rate of uplift of 19 mm/yr obtained from InSAR data spanning 1993–1998 [*Feigl et al.*, 2000], predicts small horizontal velocities in the western part of the SISZ due to the Hengill inflation (white arrows in Figure 2). We therefore neglect the stations near Hengill to estimate a smooth preseismic velocity field.

[8] Not all the GPS stations were occupied on two separate occasions before the earthquakes in 2000. Interseismic horizontal velocities at these stations were estimated by interpolation (Delaunay triangulation) of neighboring station velocities with preseismic uncertainties lower than 4 mm/yr. This procedure yields a smooth preseismic velocity field that is valid even for the stations affected by the 1993–1998 inflation episode at Hengill (Table S1 and white arrows in Figure 3). A similar interpolation of the vertical preseismic velocity field is not reasonable in light of the large uncertainties in the velocity estimates and perturbations caused by the Hengill inflation prior to the June 2000 earthquake sequence. The details of the preseismic velocity field in SW Iceland are described in a separate study (Árnadóttir et al., submitted manuscript, 2005).

4. Postseismic Velocities in the SISZ

[9] We correct the postseismic velocities for secular plate motion by subtracting the estimated interseismic horizontal velocity field from the year-to-year solutions. We therefore assume that the background plate spreading was not perturbed by the earthquakes and remains unchanged during the postseismic interval. We do not, however, make a

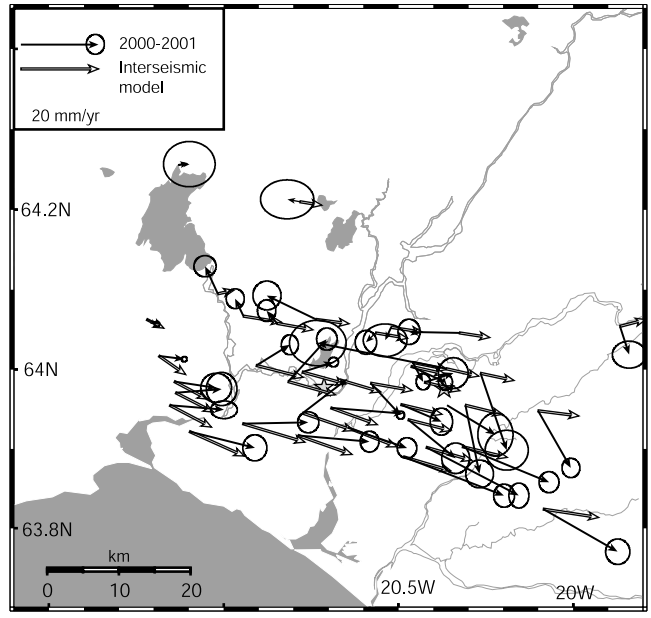

Figure 3. Horizontal GPS velocities during the first year (2000–2001) (black arrows with 68% confidence ellipses) in comparison to estimated interseismic plate velocities (white arrows). All velocities are shown relative to REYK.

[1]Auxiliary material is available at ftp://ftp.agu.org/apend/jb/2005JB003701.

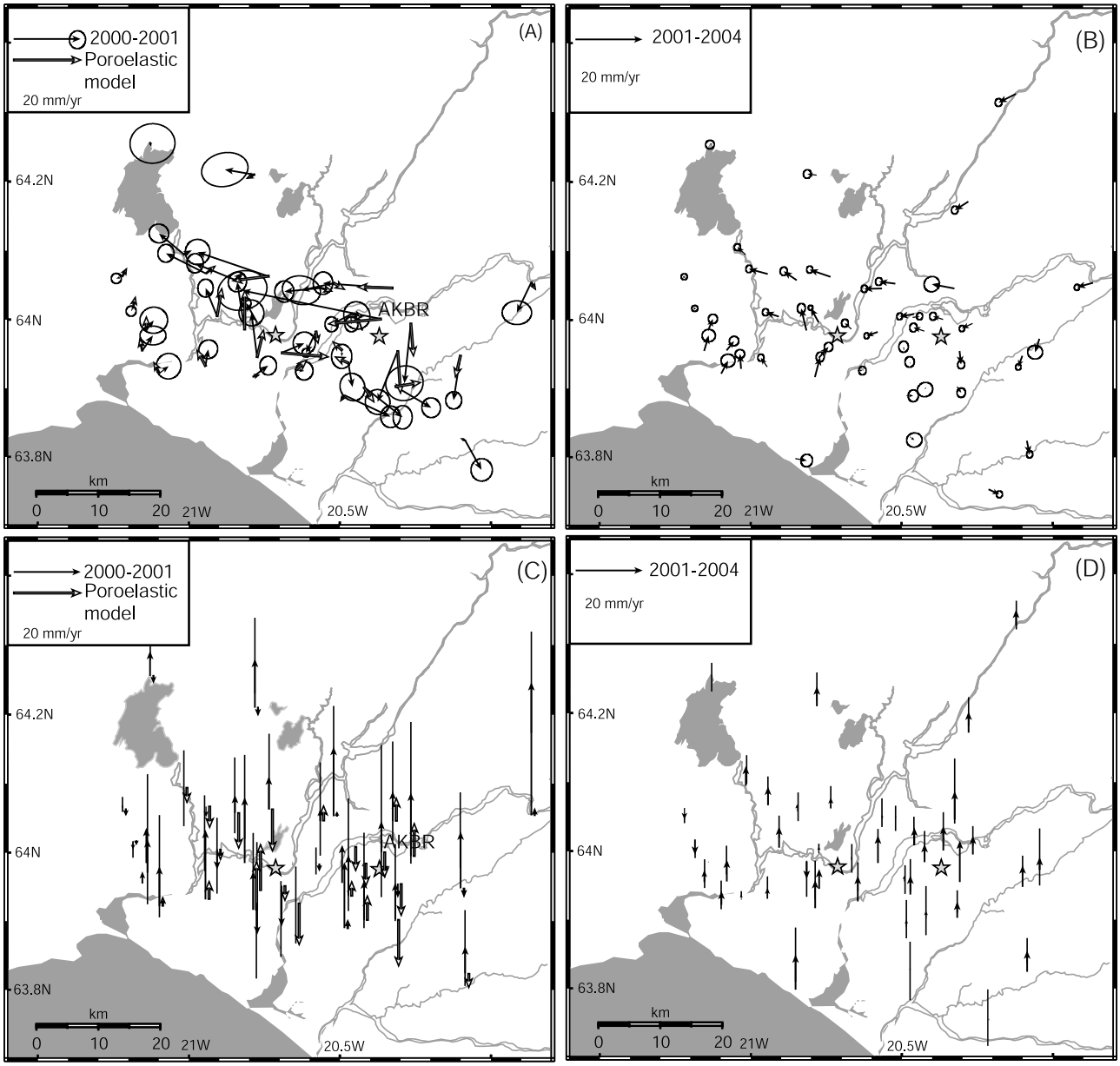

Figure 4. Postseismic GPS station velocities (black arrows with 68% confidence ellipses) corrected for interseismic plate motion. (a) Horizontal velocity field for 2000–2001. Motion predicted by a model of poroelastic relaxation is shown with white arrows [*Jónsson et al.*, 2003]. (b) Horizontal velocity field for 2001–2004. (c) Vertical postseismic GPS station velocities for 2000–2001 (in ITRF2000), with poroelastic model prediction (white arrows). (d) Vertical velocities for 2001–2004 (in ITRF2000).

similar correction to the vertical velocities as we do not have robust estimates of vertical velocities for the preseismic interval at most of our stations in the SISZ. The vertical velocities shown in all figures are in the ITRF2000 reference frame. The signal-to-noise ratio of the annual postseismic velocities is low (Figure 4). In addition, the velocity estimates appear to be rather variable from one year to another, e.g., for the 2002–2003 and 2003–2004 intervals, where the time between the observations is less than one year. Inspection of the postseismic station time series suggests that the velocities do not decay rapidly from 2001 to 2004. We therefore divide the postseismic time series into two intervals: 2000–2001 when the postseismic signal appears to be larger than for the other intervals and 2001–2004 interval when postseismic velocities appear relatively stable (Figure 4). We interpret the velocities from these two time intervals in the remainder of this paper.

[10] The general pattern of the postseismic displacements shows stations to the west of the 21 June rupture moving northward, turning more westward north of the two ruptures, whereas stations to the east of the 17 June rupture move southwest to southward (Figure 4). Velocities of the stations in the area between the faults are small. The vertical velocity pattern is less clear, with most stations showing uplift (Figure 4). We exclude vertical data from the easternmost stations (THJO and ISAK) in our analysis as the

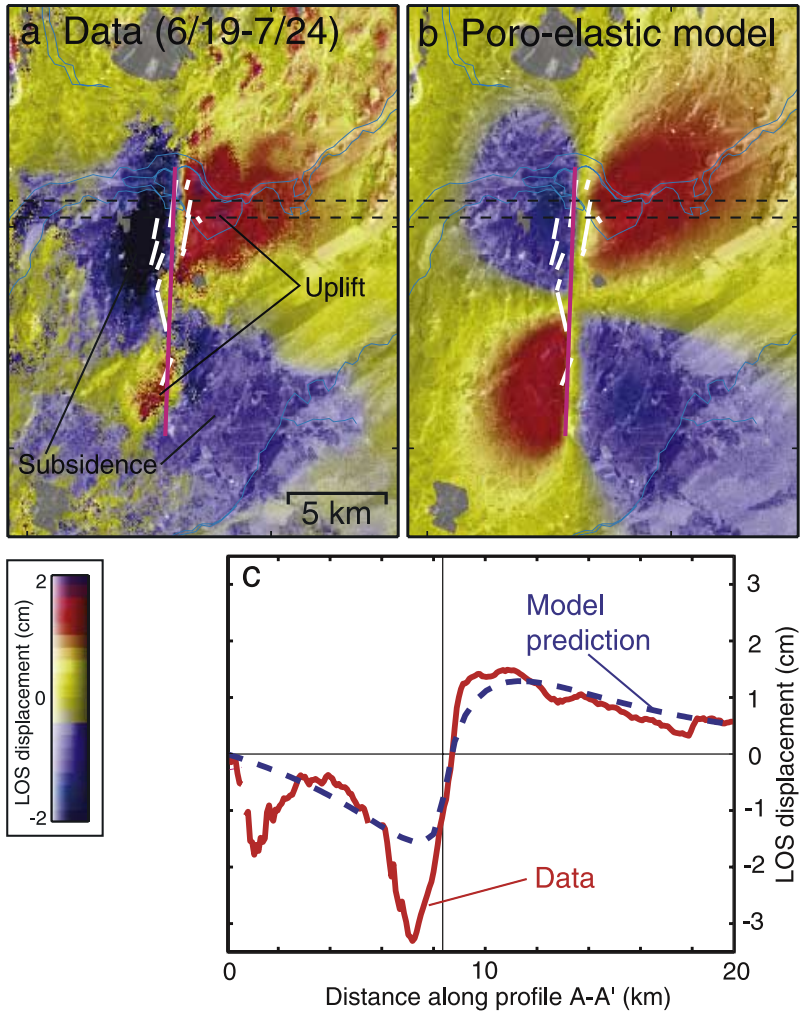

Figure 5. (a) Synthetic aperture radar interferogram (InSAR) showing near vertical postseismic displacements in the line of sight (LOS) toward the satellite near the 17 June rupture from 19 June to 24 July 2000. (b) Simulated interferogram assuming poroelastic relaxation. (c) Average LOS displacement in an E-W profile for interferogram shown in Figure 5a, drawn with the red curve, and the model prediction in Figure 5b with blue. After Figure 2 of *Jónsson et al.* [2003].

high vertical velocity is probably due to reinflation of the Hekla volcano following its eruption in February 2000 [*Ágústsson et al.*, 2000].

5. Poroelastic Transient

[11] A rapid postseismic deformation transient was observed in satellite radar interferograms (InSAR) near the 17 and 21 June surface ruptures during the first 2 months after the earthquakes [*Jónsson et al.*, 2003]. The InSAR data record changes in distance along the near-vertical line of sight between the ground and the ERS-2 satellite between 19 June and 24 July. The observed deformation pattern shows four quadrants around the 17 June rupture (Figure 5a). Postseismic subsidence is observed in the coseismically compressive quadrants NW and SE of the ruptures, while postseismic uplift is found in the coseismically extensional quadrants. This near-field deformation decayed rapidly, vanishing within about 2 months [*Jónsson et al.*, 2003].

[12] This short-term, near-field deformation signal cannot be explained by deep rooted mechanisms such as viscoelastic relaxation in the lower crust and upper mantle or by postseismic afterslip occurring below the coseismic fault slip [*Jónsson et al.*, 2003]. The deformation pattern is, however, consistent with models of poroelastic rebound in the crust due to postearthquake changes in pore pressure (Figure 5b). For this model calculation we assume a poroelastic crust that changes from an undrained state (Poisson's ratio of $\nu_u = 0.31$) just after the earthquakes to a fully drained state ($\nu = 0.27$) where all the earthquake-induced groundwater pressure changes have dissipated. This model also assumes the coseismic slip distributions estimated for the 17 and 21 June main shocks from a joint inversion of the coseismic GPS and InSAR measurements [*Pedersen et al.*, 2003]. Both the magnitude and pattern of the deformation predicted from this model agree well with the InSAR data (Figure 5a). In addition, this interpretation is supported by water level observations from numerous geothermal wells in the region. The spatial distribution of

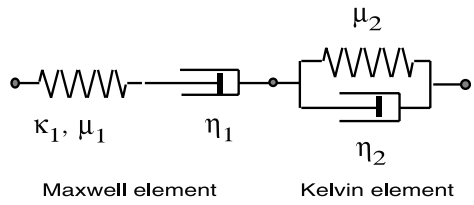

Figure 6. A transient rheology as represented by a Burgers body. It consists of a Maxwell element in series with a Kelvin element, which are characterized by steady state shear and bulk moduli μ_1 and κ_1, respectively, steady state viscosity η_1, transient viscosity η_2, and transient shear modulus μ_2. If $\eta_1 = \infty$, then the material behaves like a standard linear solid with relaxed shear modulus $\mu' = \mu_1\mu_2/(\mu_1 + \mu_2)$. If $\eta_2 = \infty$ or $\mu_2 = \infty$, then the material behavior reduces to a Maxwell rheology.

the postseismic water level changes is consistent with the observed rebound as the water level recovered in most wells within 1–2 months [*Jónsson et al.*, 2003].

[13] We use this poroelastic model to calculate displacements at our GPS stations and to correct the 2000–2001 GPS velocities for this effect. The largest predicted displacements are within 5 km of the fault ruptures, explaining a significant part of the observed velocities at these stations (white arrows in Figures 4a and 4c and Table S4, auxiliary material). The vertical signal correlates less well with the poroelastic model than the horizontal, with some stations showing uplift where the model predicts subsidence. In particular at station AKBR, near the northern end of the 17 June fault, the model explains only a fraction of the observed velocity, although the azimuth is not far off. In the area northwest of the 17 June rupture the poroelastic model also underpredicts the InSAR observations, possibly because of inhomogeneous rheological properties there (Figure 5c). This GPS station (AKBR) may also have been affected by anelastic deformation due to surface cracks observed close to the station and we therefore exclude it from our interpretations. For the remaining GPS stations, we subtract the poroelastic model predictions from the 2000–2001 velocity field. We use this corrected velocity field in our modeling of the longer term postseismic deformation in the following sections.

6. Viscoelastic Relaxation

[14] To explain the year-scale transients observed in the postseismic velocity fields, we explore a transient rheology. The simplest form of a transient rheology is a Burgers body, as shown in Figure 6. This is a linear biviscous model consisting of a Maxwell element in series with a Kelvin element. Five parameters are needed to parameterize the rheology of such a material: the steady state shear modulus μ_1, the steady state bulk modulus κ_1, the steady state viscosity η_1, the transient shear modulus μ_2, and the transient viscosity η_2. This rheology allows for an initial transient response associated with relaxation time $\tau_2 = \eta_2/\mu_2$ followed by a slower steady state response associated with relaxation time $\tau_1 = \eta_1/\mu_1$, for suitable choices of $\eta_2 \ll \eta_1$. The details of the equations governing the Burgers body are given by *Pollitz* [2003]. It is useful to note that the response at times that are long compared with τ_2, but short compared with τ_1, is equivalent to the elastic response with modified shear modulus $\mu' = \mu_1\mu_2/(\mu_1 + \mu_2)$. If either $\eta_2 = \infty$ or $\mu_2 = \infty$, the material behavior reduces to that of a Maxwell rheology. Several studies have used this type of transient rheology to describe crustal deformation [e.g., *Peltier et al.*, 1981; *Yuen et al.*, 1986]. *Bills et al.* [1994] explored millennium-scale crustal asthenospheric relaxation following unloading of lacustrine loads in the western United States, employing a Burgers body rheology for the mantle. *Ivins* [1996] explored the possibility of transient rheology in the lower crust of the Mojave Desert, California in order to explain rapid postseismic deformation observed for the first 3 months following the 1992 $M = 7.4$ Landers earthquake. *Pollitz* [2003] examined the time-dependent GPS velocity field around the region of the 1999 $M = 7.1$ Hector Mine, California earthquake, finding that both horizontal and vertical deformation patterns could be well explained by predominantly viscoelastic relaxation of a mantle, modeled as a Burgers body with material relaxation times of 0.07 and 2 years. Unlike earlier crustal deformation studies, *Pollitz* [2003] isolated the transient rheology to be a mantle phenomenon, dominating any possible transient rheology in the lower crust. A similar conclusion is reached by *Pollitz* [2005] in the area of the 2002 Denali, Alaska, earthquake, where the temporal pattern and observation of anomalously rapid horizontal postseismic movements at great distance from the rupture again point to a transient rheology in the mantle. It is not clear if a transient rheology or a stress- and temperature-dependent nonlinear rheology [*Freed and Bürgman*, 2004] best characterizes the mantle. It is also unknown if a transient rheology applies to Earth's upper mantle globally. It is, however, consistent with the expected initial rapid transient response followed by a transition from anelastic to viscous deformation mechanisms, based on laboratory constraints [e.g., *Minster and Anderson*, 1981].

[15] The present SISZ data set is not sufficient to independently constrain a transient rheology in Iceland. We therefore follow earlier studies and adopt a layered viscoelastic structure with a Maxwell rheology with viscosity η_c for the lower crust, and a Burgers body rheology with a steady state viscosity η_1 for the mantle below the SISZ (Figure 7). We assume an elastic upper crust down to 10 km, based on the depth extent of earthquake hypocenters in the SISZ [e.g., *Stefánsson et al.*, 1993; *Tryggvason et al.*, 2002], and a lower crust from 10–20 km consistent with estimates of Moho depth from seismic studies [e.g., *Bjarnason et al.*, 1993b; *Allen et al.*, 2002]. On the basis of inferred mantle rheology from previous studies applying a Burgers body rheology [*Pollitz*, 2003, 2005], we assume a transient mantle viscosity that scales with the steady state viscosity, such that $\eta_2 = \eta_1 \times 0.036$. We also assume that $\mu_2 = \mu_1$, then $\mu' = 0.5 \times \mu_1$.

[16] Predicted viscoelastic relaxation is controlled by source models of the 17 and 21 June events [*Árnadóttir et al.*, 2001] combined with the depth distribution of viscoelastic parameters. We employ the method of *Pollitz* [1997] to compute the globally valid viscoelastic surface deformation fields at specific points and given time interval. The

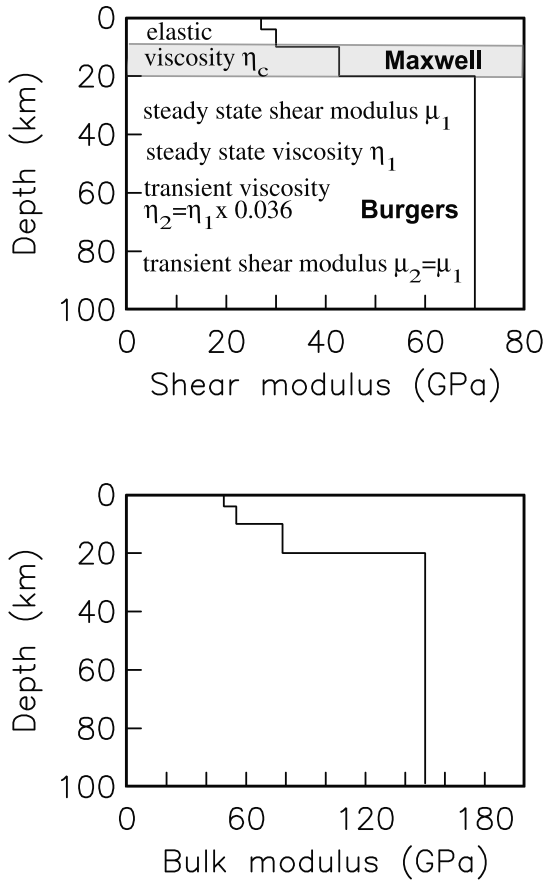

Figure 7. Layered Earth model for the SISZ used in this study. We assume an elastic upper crust down to 10 km, based on average depth of earthquake hypocenters in the SISZ, and a lower crust from 10 to 20 km consistent with seismic studies. On the basis of similar studies [*Pollitz*, 2003, 2005] we assume a Maxwell and Burgers body rheology for the lower crust and upper mantle, respectively. In order to reduce the number of unknowns we adopt scalings among these parameters determined by *Pollitz* [2003] for the upper mantle beneath the Mojave Desert, i.e., values of the ratio μ_2/μ_1 and ratio η_2/η_1.

model velocity field depends on both the viscoelastic parameters as well as a velocity shift:

$$\mathbf{v}_j(\mathbf{r}_i) = \mathbf{v}_j^{\mathrm{VE}}(\mathbf{r}_i) + \boldsymbol{\Delta} v_j \tag{1}$$

where $\mathbf{v}_j(\mathbf{r}_i)$ is the total calculated surface velocity field at site i and time interval j, $\mathbf{v}_j^{\mathrm{VE}}(\mathbf{r}_i)$ is the contribution of viscoelastic relaxation, and $\boldsymbol{\Delta}\mathbf{v}_j$ is the velocity shift vector for that time interval. This velocity shift is meant to account for possible long-wavelength inaccuracies in the interseismic correction, including a background uplift signal.

[17] For time interval j the misfit function is defined as

$$\chi_j^2 = \mathbf{q}_j^T \cdot \mathbf{C}_j{}^{-1} \cdot \mathbf{q}_j \tag{2}$$

where, for each time interval j, the residual column vector $\mathbf{q}_j$ is obtained by taking the difference between the observed velocity field $\mathbf{u}_{ji}$ at site i and the model prediction $\mathbf{v}_j$ ($\mathbf{r}_i$) at that site, and $\mathbf{C}_j$ is the associated data covariance matrix. The residual vector $\mathbf{q}_j$ has three components from each site for a total of $3n$ components, where n is the total number of sites.

[18] We minimize the misfit by varying both η_c and η_1 in a grid search. Figure 8 shows the fit of model velocity fields to observed 2000–2001 and 2001–2004 velocity fields, separated into the horizontal and vertical components. The misfit for a given model is shown with respect to both η_c and η_1, the former being represented by the ratio η_c/η_1. A line with a slope of -1 on these plots represents models with constant η_c. For the horizontal velocity field, it is clear that low-misfit models tend to fall on such a line, corresponding to $\eta_c \sim 0.5$–1×10^{19} Pa s and admissible η_1 values over a broad range from 10^{18} to 10^{20} Pa s. Thus, even allowing for possible complexity in the mantle postseismic response, we find that the horizontal GPS measurements following the 17 and 21 June SISZ events constrain lower crust viscosity to within a factor of about 2. To attempt to constrain η_1, we note that theoretically the vertical velocity field is very sensitive to the ratio η_c/η_1. A ratio $\gtrsim 3$ is weakly suggested by the vertical χ^2 misfit pattern (Figure 8d). The horizontal χ^2 values are lowest for ratios $\eta_c/\eta_1 \lesssim 3$. Together with the vertical misfit patterns this suggests that $\eta_c \sim 3 \times \eta_1$. We thus have a slight preference for a rheology with the following parameters: $\eta_1 = 3 \times 10^{18}$ Pa s, $\eta_2 = 1.0 \times 10^{17}$ Pa s, $\eta_c = 1.0 \times 10^{19}$ Pa s, $\mu_2 = \mu_1 = 70$ GPa. This combination of parameters is indicated by the black circles on the plots of Figure 8. Comparison of the vertical rates for the preferred low-η_1 model and an alternative high-η_1 model, which is also consistent with the horizontal postseismic velocity pattern (indicated by black triangles in Figure 8), gives a correlation coefficient between predicted and observed uplift of 0.11 and -0.18 for the low-η_1 and high-η_1 models, respectively. Although the vertical postseismic signal is greatly contaminated by noise, we believe that this provides a useful constraint on the rheology.

[19] We compare predicted viscoelastic and observed horizontal velocity fields for the two postseismic time intervals in Figures 9a–9b using this preferred model. Both the pattern and amplitude of elevated postseismic velocities, particularly the factor of two reduction in velocities between 2000–2001 and 2001–2004, are matched by the viscoelastic model. To assess how well the models fit the data we calculate the weighted RMS residuals as WRMS = $\sqrt{(\chi^2/N)}$, where χ^2 is calculated from equation (2), and N is the number of data. Here N = 42 stations × 3 components (=126) for the first year and 53 stations × 3 components (=159) for the 2001–2004 time interval. The WRMS is 2.0 for the horizontal velocities during the first year and 2.2 for the later time interval. In Figures 9c–9d we compare predicted and observed uplift for the preferred low-η_1 model. Because of the large uncertainties in the vertical GPS velocities during the first year, the WRMS misfit is 1.2 compared to 1.5 for the 2001–2004 interval, although visually the agreement between the observations and model is better for the latter time interval.

[20] The choice of mantle rheology and viscosity influences the estimation of η_c. If η_1 were sufficiently high ($\eta_1 \gg 10^{19}$ Pa s), then mantle flow would be controlled almost entirely by the Kelvin element during the first 4 years. The mantle during times $t \ll \tau_1$ would then behave as a standard linear solid (SLS), and during the transient period

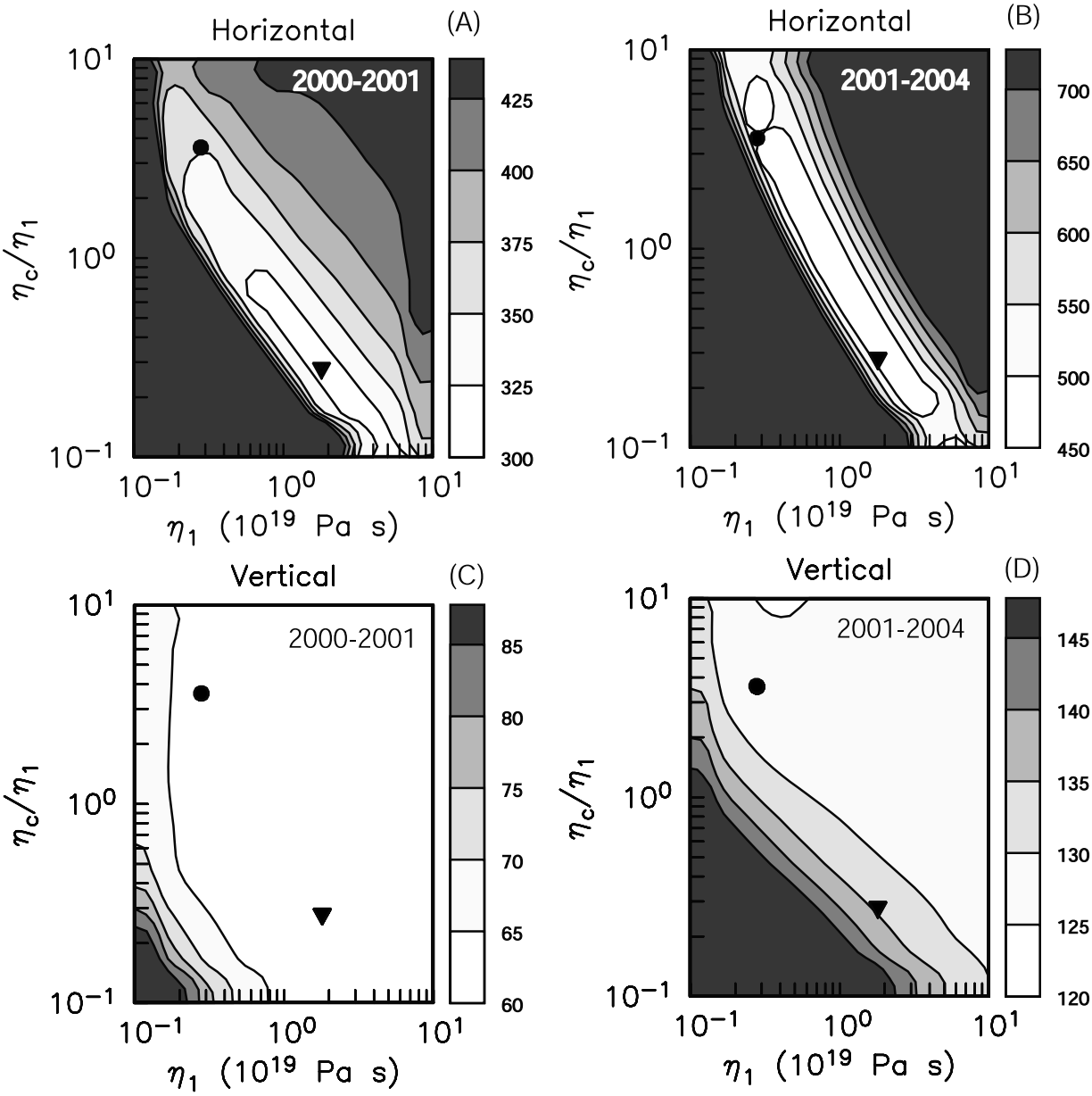

Figure 8. Residual misfit of a set of viscoelastic models with respect to observed velocities in two time intervals. This is calculated from equation (2) (a and b) for the horizontal velocity components and (c and d) for the vertical velocity components. Black circles and triangles indicate the preferred low-η_1 model and an alternative high-η_1 model.

($t \lesssim \tau_2$) the mantle would gradually relax to a lowered shear modulus of μ' with an exponential decay time of τ_2 [see *Pollitz*, 2003, equation 2]. Thus the admissible models in Figure 8, near $\eta_1 \sim 5 \times 10^{19}$ Pa s, $\eta_c/\eta_1 = 0.1$, where misfit is low, suggest that inferred crust viscosity is $\eta_c \sim 5 \times 10^{18}$ Pa s for an effectively SLS mantle rheology. For smaller η_1, inferred η_c tends to be larger, i.e., $\eta_c \sim 7 \times 10^{18}$ Pa s for $\eta_1 \sim 10^{19}$ Pa s, and $\eta_c \sim 10^{19}$ Pa s for $\eta_1 \sim 3 \times 10^{18}$ Pa s. In a previous study, *Árnadóttir et al.* [2003b] found that inferred η_c is in the range $2-4 \times 10^{18}$ Pa s and nearly independent of η_1 when a Maxwell rheology is prescribed for the mantle ($\eta_2 = \infty$ and η_1 variable). This shows that the inferred η_c not only depends upon the choice of mantle rheology but also, in the case of a transient rheology, trades off somewhat with mantle viscosity. Note that all transient rheologies considered here have $\eta_1 \leq 10^{20}$ Pa s and thus $\eta_2 \leq 3.6 \times 10^{18}$ Pa s, corresponding to $\tau_2 \leq 1.6$ years. The two candidate models considered in Figure 8 are associated with material relaxation times $\eta_c/\mu_c \sim 10$ years in the lower crust and $\tau_2 = 0.05$ years or 0.3 years and $\tau_1 = 1.3$ years or 8 years in the mantle. Thus the observed rapid decrease in postseismic velocities between 2000 and 2004 is largely attributed to the influence of mantle relaxation in the viscoelastic models.

7. Afterslip

[21] We now investigate if postseismic slip (afterslip) on narrow shear zones in the lower crust, below the coseismic

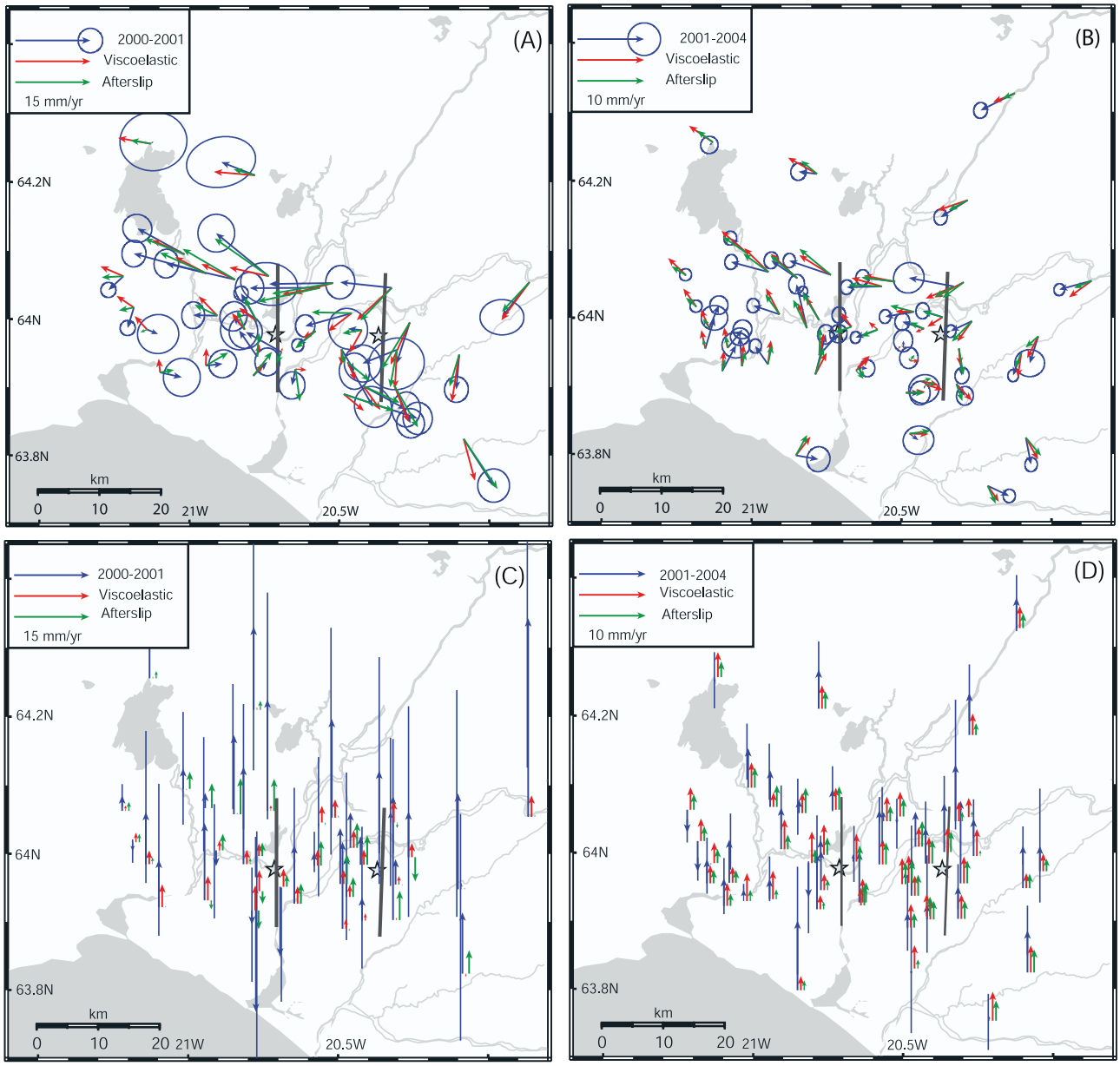

Figure 9. Observed (black arrows with 68% confidence ellipses) and calculated velocity fields for the preferred viscoelastic model (black circles in Figure 8), shown with light gray arrows. The velocities predicted by the best fit afterslip models (Figure 10) are shown with dark gray arrows (with no error ellipses). The bold gray lines denote the updip surface projection of the afterslip fault models. The horizontal velocity field for (a) the 2000–2001 interval, (b) the 2001–2004 interval. The vertical velocity field for observed (blue arrows), preferred viscoelastic model (red arrows) and optimal afterslip models (green arrows) (c) 2000–2001, and (d) 2001–2004. The model velocity fields have been corrected for the estimated shift of $\mathbf{\Delta v}$ (equation (1)), which is approximately 1–2 mm/yr in horizontal and 2–3 mm/yr in vertical.

ruptures, can provide an alternative mechanism to viscoelastic relaxation. Afterslip has been suggested as an explanation for observed postseismic deformation in a variety of tectonic settings, e.g., after major strike-slip earthquakes such as the 1999 Izmit, Turkey, earthquake [*Reilinger et al.*, 2000; *Bürgmann et al.*, 2002; *Ergintav et al.*, 2002] and following shallow reverse faulting events like the 1999 Chi-Chi, Taiwan earthquake [*Hsu et al.*, 2002; *Perfettini and Avouac*, 2004]. In addition, deformation transients observed after large subduction earthquakes are usually thought to be caused by afterslip on the subduction interface [e.g., *Heki et al.*, 1997].

[22] Here we estimate afterslip directly from the observed postseismic GPS data in a similar fashion as coseismic fault slip is derived. We use fault locations and geometries determined by *Pedersen et al.* [2003] from GPS and InSAR data, extend these faults well into the lower crust and divide them into multiple rectangular subfaults. We then use the

postseismic GPS data to invert for spatially variable afterslip during the two time intervals 2000–2001 and 2001–2004, assuming elastic rheology [*Okada*, 1992]. Following equation (1), the modeled velocity field at site i for time interval j

$$\mathbf{v}_j(\mathbf{r}_i) = \mathbf{v}_j^{\mathrm{AS}}(\mathbf{r}_i) + \boldsymbol{\Delta}\mathbf{v}_j \quad (3)$$

is the sum of the velocity prediction due to distribution of afterslip $\mathbf{v}_j^{\mathrm{AS}}(\mathbf{r}_i)$ and an estimated velocity shift vector $\boldsymbol{\Delta}\mathbf{v}_j$, as explained in section 6. We minimize the misfit function in equation (2) using a nonnegative least squares approach, i.e., allowing only right-lateral afterslip. In addition, we apply smoothing to the solution, but otherwise put no restrictions on where on the fault planes afterslip can take place.

[23] For the 2000–2001 time interval the estimated afterslip is concentrated at depths 8–14 km with a maximum of 40 cm/year on each fault. The afterslip occurs below regions with numerous aftershocks and its distribution appears to be a downward continuation of the coseismic fault slip as observed in other strike-slip earthquakes (e.g., Izmit 1999 [*Reilinger et al.*, 2000]) (Figure 10). A small amount of shallow afterslip is found near the southern and northern end of the 21 June coseismic rupture which correlates well with the extent of aftershocks. The predicted GPS displacements from this afterslip model explain the main features in the observed GPS displacement field (Figure 9). The weighted RMS for the optimal afterslip model is 1.4 and 1.1 for the horizontal and vertical components, respectively for the first year compared to 1.9 and 1.7 for the horizontal and vertical components, respectively for the later interval.

[24] The optimal distribution of afterslip for the 2001–2004 interval is less convincing. In this case afterslip is found at shallower depths as well as having two clear slip maxima on each fault plane (Figure 10). If afterslip was driven by the rather smooth coseismic fault slip distribution, then multiple afterslip maxima seem unlikely. These afterslip maxima, however, appear to the north and to the south of the afterslip maxima found for the earlier interval in 2000–2001 on both faults. Therefore one could argue that afterslip first occurred directly below the coseismic slip and then propagated both to the south and to the north.

8. Discussion

[25] Several previous studies have advocated for afterslip being the main postseismic mechanism for large ($M_w \gtrsim 7$) strike-slip earthquakes [e.g., *Hearn*, 2003], while some other studies have concluded that viscoelastic relaxation is the dominant mechanism [e.g., *Pollitz et al.*, 2001; *Pollitz*, 2003, 2005; *Freed and Bürgman*, 2004]. The observed postseismic deformation in the SISZ does not clearly favor one of these two mechanisms; both seem equally likely. The GPS velocity field shows an overall right-lateral motion and suggests uplift across the whole area (Figure 9). While the horizontal velocity pattern may either be caused by afterslip below the coseismic ruptures or by viscoelastic relaxation, neither mechanism can fully explain the observed vertical velocity field, despite allowing for a vertical shift of about 2–3 mm/yr in the modeling. A direct comparison of the model fits for the viscoelastic and afterslip models is not straightforward, as smoothing and nonnegativity constraints in the afterslip modeling reduce the number of independent model parameters considerably. In general one would expect a lower misfit for the afterslip models than the viscoelastic model, since the former has many more model parameters; 283 instead of only 5 for the viscoelastic model. The data alone (i.e., a null model) give rise to a WRMS of 2.6 for the first year (2000–2001) and 3.3 for later time interval (2001–2004). The WRMS for the viscoelastic model is 1.8 for the first year compared to 2.0 for the later interval, whereas the weighted RMS for the optimal afterslip model is 1.3 for the first year, compared to 1.8 for the later interval. The estimated distribution of afterslip appears more plausible during the first year than for the latter time interval. Therefore we suggest that viscoelastic relaxation and afterslip occurred during the first year, but viscoelastic relaxation was the dominant mechanism during the later years. A more sophisticated model using numerical methods to allow for all three processes (i.e., poroelastic and viscoelastic relaxation and afterslip) to be active simultaneously during the first year, is outside the scope of our study.

[26] Several studies estimating the rheological properties under Iceland from geodetic data have been published. A range of viscosities from 1×10^{18} to 5×10^{19} Pa s (under a 10 km thick elastic crust) was deduced from lake tilt measurements using a model of glacial rebound due to shrinking of Vatnajökull, Iceland's largest glacier [*Sigmundsson and Einarsson*, 1992]. GPS measurements in north Iceland have shown a large continuing rift-normal extension away from the plate boundary, following the Krafla rifting episode that took place in 1975–1984 [*Björnsson*, 1985]. This extension has been interpreted as being predominantly due to postrifting stress relaxation after the rifting episode. *Heki et al.* [1993] found that displacements observed in northern Iceland from 1987 to 1990 are consistent with a two-dimensional model of a thin elastic plate over a viscous layer with a Newtonian viscosity of $0.3–2 \times 10^{18}$ Pa s. A similar value of 1.1×10^{18} Pa s was estimated using GPS data from 1987–1992 and a model consisting of 10 km thick elastic crust overlaying a viscoelastic half-space [*Hofton and Foulger*, 1996]. *Pollitz and Sacks* [1996] applied a layered viscoelastic model to the same data set and found lower crustal and upper mantle viscosities of 3×10^{19} Pa s and 3×10^{18} Pa s, respectively. A study of GPS velocities from 1994 to 2003 across the western and eastern volcanic zones, assuming a Maxwell rheology in a half-space below an elastic plate, suggests viscosities of 4×10^{19} Pa s [*LaFemina et al.*, 2005]. Our preferred viscoelastic relaxation model for the SISZ is similar to that of *Pollitz and Sacks* [1996], with lower crustal viscosity of $0.5–1 \times 10^{19}$ Pa s and upper mantle viscosity of about 3×10^{18} Pa s.

[27] An outstanding question is whether or not the postseismic processes after the June 2000 earthquakes have increased the stress on faults in the SISZ. Large earthquakes in the SISZ tend to occur in sequences on several parallel N-S striking faults that are separated by 15–20 km. These sequences typically begin in the east and then progress to the west. As the June 2000 sequence consisted of only two earthquakes, it is important to study stress changes on N-S striking faults located 15–20 km to the west of the 21 June rupture, and also to the east of the 17 June rupture, which are

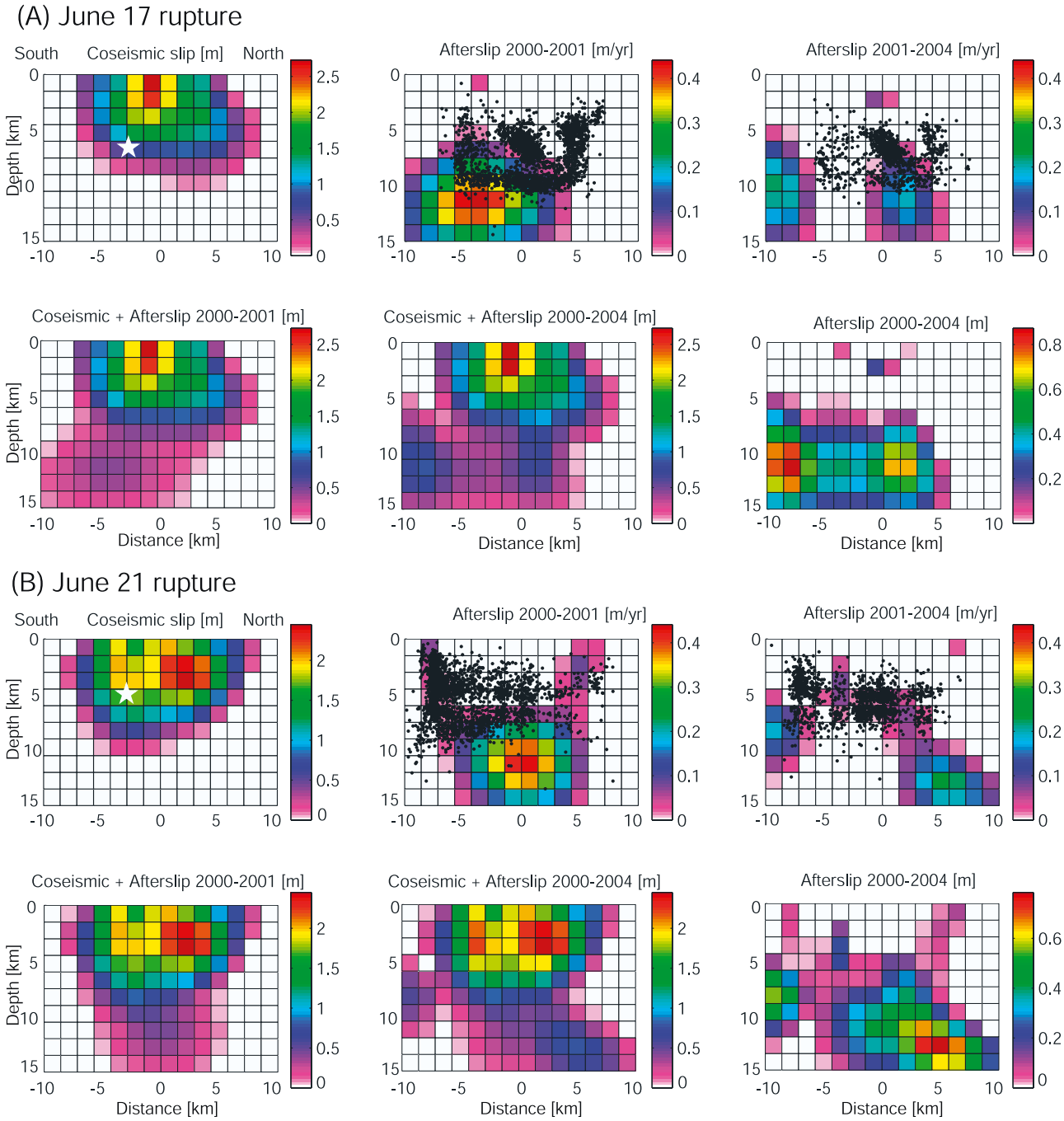

Figure 10. Distributed slip models for the (a) 17 June rupture and (b) 21 June rupture. Afterslip models for the different intervals (2000–2001 and 2001–2004) are shown in the top middle and right panels, respectively. The coseismic slip distribution is shown in the top left panel. The bottom three panels show the cumulative slip for the different time intervals, i.e., coseismic and first year of postseismic slip (left), coseismic and first 4 years of postseismic slip (middle) and total afterslip (right). The black dots are earthquake hypocenters recorded by the SIL seismic network during the two time intervals (B. Thorbjarnardóttir, personal communication, 2004).

the most likely locations of the next large earthquake. Coseismic Coulomb failure stress (CFS) change calculations indeed show significant positive CFS changes in these areas, indicating that dextral N-S striking faults at these locations were brought closer to failure [*Árnadóttir et al.*, 2003a]. Stress calculations using our preferred afterslip models reveal a similar pattern of CFS changes suggesting that afterslip would further load these faults by ~0.05 MPa. Similarly, our optimal viscoelastic model predicts an overall ~0.02–0.06 MPa stress increase in the epicentral area with positive changes extending about 20 km to the east and west from the main shock ruptures. Therefore both postseismic mecha-

nisms appear to further load favorably oriented faults to the west and to the east of the June 2000 main shock faults.

[28] The total geodetic moment of the two M_w = 6.5 June 2000 earthquakes has been estimated $\sim 1 \times 10^{19}$ N m [*Árnadóttir et al.*, 2001; *Pedersen et al.*, 2003] using $M_0 = \mu Au$, where μ is the shear modulus, A fault area, and u mean slip. *Sigmundsson et al.* [1995] used the rate of geometric moment, $\dot{M}_0/\mu$, as a measure to compare the rate of moment buildup in the SISZ due to plate spreading, estimated as $1.0-2.5 \times 10^7$ m^3/yr, to the rate of seismic moment release in historical times, estimated as $2.0-2.3 \times 10^7$ m^3/yr [*Stefánsson and Halldórsson*, 1988; *Hackman et al.*, 1990]. The geometric moment of the two June 2000 main shocks is about 3×10^8 m^3, whereas the moment built up since the M_S = 7.0 earthquake in 1912 is $9-22 \times 10^8$ m^3 [*Pedersen et al.*, 2003]. The June 2000 main shocks therefore released at most only one third of the moment built up due to plate spreading in the previous 88 years. Our afterslip model adds about 1×10^8 m^3, over the 4 years that our data spans. We therefore conclude that there is still a significant amount of moment stored in the brittle crust in the SISZ, suggesting that we may expect large earthquakes there in the near future. Our stress change calculations indicate that the areas west of the 21 June rupture and east of the 17 June rupture remain the most likely areas of future earthquakes.

9. Conclusions

[29] Postseismic deformation observed with GPS in the SISZ after two M_w = 6.5 earthquakes is modeled using viscoelastic rheology and afterslip. The optimal afterslip models have slip at 8–14 km depth below the coseismic ruptures during the first year and slip extending farther north and south during the succeeding three years. The preferred viscoelastic relaxation model has a lower crustal viscosity of about 10^{19} Pa s, and a poorly constrained mantle viscosity of 3×10^{18} Pa s. This is based on joint consideration of a robust horizontal velocity field and a marginally significant vertical velocity field. Consideration of the horizontal velocity data alone constrains the lower crustal viscosity to the range $0.5-1 \times 10^{19}$ Pa s. Given the different number of parameters used in the two types of models, it is difficult to favor one model over another on the basis of misfit alone. Both types of postseismic deformation models suggest that the areas east of the 17 June and west of the 21 June ruptures, that had a large coseismic stress increase, continue to be loaded by the postseismic deformation.

[30] **Acknowledgments.** We are grateful for the invaluable contribution made by the numerous people collecting the vast amount of GPS campaign data used in this study. This work has benefited from discussions with Halldór Geirsson, Sigrún Hreinsdóttir, and Freysteinn Sigmundsson. Comments from Giorgio Spada and two anonymous reviewers helped us to improve the text. B. Thorbjarnardóttir at the Icelandic Meteorological Office provided the hypocenter locations shown in Figure 10. This work was supported in part by the Icelandic Research Council grant 031590003, EU contract EVG1-CT-2001-0044 (RETINA), and EU contract EVG1-CT-2002-00073 (PREPARED). The European Space Agency provided the SAR data. Many of the figures were produced using the GMT public domain software [*Wessel and Smith*, 1998].

References

Ágústsson, K., R. Stefánsson, A. T. Linde, P. Einarsson, I. S. Sacks, G. B. Gudmundsson, and B. Thorbjarnardóttir (2000), Successful prediction and warning of the 2000 eruption of Hekla based on seismicity and strain changes, *Eos Trans. AGU*, *81*(48), Fall Meet. Suppl., Abstract V11B-30.

Allen, R. M., et al. (2002), Plume-driven plumbing and crustal formation in Iceland, *J. Geophys. Res.*, *107*(B8), 2163, doi:10.1029/2001JB000584.

Altamimi, Z., P. Sillard, and C. Boucher (2002), ITRF2000: A new release of the International Terrestrial Reference Frame for earth science applications, *J. Geophys. Res.*, *107*(B10), 2214, doi:10.1029/2001JB000561.

Árnadóttir, T., S. Hreinsdóttir, G. Gudmundsson, P. Einarsson, M. Heinert, and C. Völksen (2001), Crustal deformation measured by GPS in the south Iceland seismic zone due to two large earthquakes in June 2000, *Geophys. Res. Lett.*, *28*(21), 4031–4034.

Árnadóttir, T., S. Jónsson, R. Pedersen, and G. B. Gudmundsson (2003a), Coulomb stress changes in the south Iceland seismic zone due to two large earthquakes in June 2000, *Geophys. Res. Lett.*, *30*(5), 1205, doi:10.1029/2002GL016495.

Árnadóttir, T., F. F. Pollitz, S. Jónsson, K. L. Feigl, E. Sturkell, H. Geirsson, and P. Einarsson (2003b), Spatiotemporal variations of post-seismic deformation after the June 2000 earthquake sequence in southwest Iceland, *Eos Trans. AGU*, *84*(46), Fall Meet. Suppl., Abstract G21B-0268.

Árnadóttir, T., H. Geirsson, and P. Einarsson (2004), Coseismic stress changes and crustal deformation on the Reykjanes Peninsula due to triggered earthquakes on 17 June 2000, *J. Geophys. Res.*, *109*, B09307, doi:10.1029/2004JB003130.

Bills, B. G., D. R. Currey, and G. A. Marshall (1994), Viscosity estimates for the crust and upper mantle from patterns of lacustrine shoreline deformation in the Eastern Great Basin, *J. Geophys. Res.*, *99*, 22,059–22,086.

Bjarnason, I., P. Cowie, M. H. Anders, L. Seeber, and C. H. Scholz (1993a), The 1912 Iceland earthquake rupture: Growth and development of a nascent transform system, *Bull. Seismol. Soc. Am*, *83*, 416–435.

Bjarnason, I. T., W. Menke, Ó. G. Flóvenz, and D. Caress (1993b), Tomographic image of the mid-Atlantic plate boundary in southwestern Iceland, *J. Geophys. Res.*, *98*, 6607–6622.

Björnsson, A. (1985), Dynamics of crustal rifting in Iceland, *J. Geophys. Res.*, *90*, 10,151–10,162.

Björnsson, G., Ó. G. Flovenz, K. Smundsson, and E. H. Einarsson (2001), Pressure changes in Icelandic geothermal reservoirs associated with two large earthquakes in June 2000, in *Proceedings of the 26th Workshop on Geothermal Reservoir Engineering*, *Tech. Rep. SGP-TR_168*, pp. 327–334, Stanford Univ., Stanford, Calif.

Bürgmann, R., S. Ergintav, P. Segall, E. H. Hearn, S. McClusky, R. E. Reilinger, H. Woith, and J. Zschau (2002), Time-space variable afterslip on and deep below the Izmit earthquake rupture, *Bull. Seismol. Soc. Am.*, *92*, 126–137.

Clifton, A. E., and P. Einarsson (2005), Styles of surface rupture analysis accompanying the June 17 and 21, 2000 earthquakes in the south Iceland seismic zone, *Tectonophysics*, *396*, 141–159.

Clifton, A. E., C. Pagli, J. F. Jónsdóttir, K. Eythórsdóttir, and K. Vogfjörd (2003), Surface effects of triggered fault slip on Reykjanes Peninsula, SW Iceland, *Tectonophysics*, *369*, 145–154.

Dziewonski, A. M., G. Ekstrom, and N. N. Maternovskaya (2001), Centroid-moment tensor solutions for April–June 2000, *Phys. Earth Planet. Inter.*, *123*, 1–14.

Einarsson, P., and J. Eiríksson (1982), Earthquake fractures in the districts Land and Rangárvellir in the south Iceland seismic zone, *Jökull*, *32*, 113–120.

Einarsson, P., S. Björnsson, G. Foulger, R. Stefánsson, and T. Skaftadóttir (1981), Seismicity pattern in the south Iceland seismic zone, in *Earthquake Prediction: An International Review*, *Maurice Ewing Ser.*, vol. 4, edited by D. W. Simpson and P. G. Richards, pp. 141–151, AGU, Washington, D. C.

Ergintav, S., et al. (2002), Postseismic deformation near the Izmit Earthquake (17 August 1999, *M*7.5) rupture zone, *Bull. Seismol. Soc. Am.*, *92*, 194–207.

Feigl, K. L., J. Gasperi, F. Sigmundsson, and A. Rigo (2000), Crustal deformation near Hengill volcano, Iceland 1993–1998: Coupling between magmatic activity and faulting inferred from elastic modeling of satellite radar interferograms, *J. Geophys. Res.*, *105*, 25,655–25,670.

Freed, A., and R. Bürgman (2004), Evidence of powerlaw flow in the Mojave desert mantle, *Nature*, *430*, 548–551.

Hackman, M. C., G. C. P. King, and R. Bilham (1990), The mechanics of the south Iceland seismic zone, *J. Geophys. Res.*, *95*, 17,339–17,351.

Hearn, E. H. (2003), What can GPS data tell us about the dynamics of postseismic deformation?, *Geophys. J. Int.*, *155*, 753–777.

Heki, K., G. R. Foulger, B. R. Julian, and C.-H. Jahn (1993), Plate dynamics near divergent boundaries: Geophysical implications of postrifting crustal deformation in NE Iceland, *J. Geophys. Res.*, *98*, 14,279–14,298.

Heki, K., S. Miyazaki, and H. Tsuji (1997), Silent fault slip following an interplate thrust earthquake at the Japan trench, *Nature*, *386*, 595–598.

Herring, T. A. (2003), GLOBK: Global Kalman filter VLBI and GPS analysis program, version 4.1, Mass. Inst. of Technol., Cambridge, Mass.

Hofton, M. A., and G. R. Foulger (1996), Postrifting anelastic deformation around the spreading plate boundary, north Iceland: 1. Modeling of the 1987–1992 deformation field using a viscoelastic Earth structure, *J. Geophys. Res.*, *101*, 25,403–25,422.

Hsu, Y., N. Bechor, P. Segall, S. Yu, L. Kuo, and K. Ma (2002), Rapid afterslip following the 1999 Chi-Chi, Taiwan earthquake, *Geophys. Res. Lett.*, *29*(16), 1754, doi:10.1029/2002GL014967.

Ivins, E. R. (1996), Transient creep of a composite lower crust, 2. A polymineralic basis for rapidly evolving postseismic deformation modes, *J. Geophys. Res.*, *101*, 28,005–28,028.

Jónsson, S., P. Segall, R. Pedersen, and G. Björnsson (2003), Post-earthquake ground movements correlated to pore-pressure transients, *Nature*, *424*, 179–183.

King, R. W., and Y. Bock (2003), *Documentation for the GAMIT Analysis Software*, release 10.1, Mass. Inst. of Technol., Cambridge, Mass.

LaFemina, P. C., T. H. Dixon, R. Malservisi, T. Árnadóttir, E. Sturkell, F. Sigmundsson, and P. Einarsson (2005), Geodetic GPS measurements in south Iceland: Strain accumulation and partitioning in a propagating ridge system, *J. Geophys. Res.*, *110*, B11405, doi:10.1029/2005JB003675.

McClusky, S., et al. (2000), Global Positioning System constraints on plate kinematics and dynamics in the eastern Mediterranean and Caucasus, *J. Geophys. Res.*, *105*, 5695–5720.

Minster, J. B., and D. L. Anderson (1981), A model of dislocation controlled rheology for the mantle, *Philos. Trans. R. Soc. London*, *299*, 319–356.

Okada, Y. (1992), Internal deformation due to shear and tensile faults in a half-space, *Bull. Seismol. Soc. Am.*, *82*, 1018–1040.

Pagli, C., R. Pedersen, F. Sigmundsson, and K. L. Feigl (2003), Triggered fault slip on June 17, 2000 on the Reykjanes Peninsula, SW-Iceland captured by radar interferometry, *Geophys. Res. Lett.*, *30*(6), 1273, doi:10.1029/2002GL015310.

Pedersen, R., F. Sigmundsson, K. L. Feigl, and T. Árnadóttir (2001), Coseismic interferograms of two M_s = 6.6 earthquakes in the south Iceland seismic zone, June 2000, *Geophys. Res. Lett.*, *28*, 3341–3344.

Pedersen, R., S. Jónsson, T. Árnadóttir, F. Sigmundsson, and K. L. Feigl (2003), Fault slip distribution of two M_w = 6.5 earthquakes in south Iceland estimated from joint inversion of InSAR and GPS measurements, *Earth Planet. Sci. Lett.*, *213*, 487–502.

Peltier, W. R., P. Wu, and D. A. Yuen (1981), The viscosities of the Earth's mantle, in *Anelasticity in the Earth*, *Geodyn. Ser.*, vol. 4, edited by F. D. Stacey, M. S. Paterson, and A. Nicholas, pp. 59–77, AGU, Washington, D. C.

Perfettini, H., and J.-P. Avouac (2004), Postseismic relaxation driven by brittle creep: A possible mechanism to reconcile geodetic measurements and the decay rate of aftershocks, application to the Chi-Chi earthquake, Taiwan, *J. Geophys. Res.*, *109*, B02304, doi:10.1029/2003JB002488.

Pollitz, F. F. (1997), Gravitational-viscoelastic postseismic relaxation on a layered spherical Earth, *J. Geophys. Res.*, *102*, 17,921–17,941.

Pollitz, F. F. (2003), Transient rheology of the uppermost mantle beneath the Mojave Desert, California, *Earth Planet. Sci. Lett.*, *215*, 89–104.

Pollitz, F. F. (2005), Transient rheology of the upper mantle beneath central Alaska inferred from the crustal velocity field following the 2002 Denali earthquake, *J. Geophys. Res.*, *110*, B08407, doi:10.1029/2005JB003672.

Pollitz, F. F., and I. S. Sacks (1996), Viscosity structure beneath northeast Iceland, *J. Geophys. Res.*, *101*, 17,771–17,793.

Pollitz, F. F., C. Wicks, and W. Thatcher (2001), Mantle flow beneath a continental strike-slip fault: Postseismic deformation after the 1999 Hector Mine earthquake, *Science*, *293*, 1814–1818.

Reilinger, R. E., et al. (2000), Coseismic and postseismic fault slip for the 17 August 1999, M = 7.5, Izmit, Turkey earthquake, *Science*, *289*, 1519–1524.

Sigmundsson, F., and P. Einarsson (1992), Glacio-isostatic crustal movements caused by historical volume change of the Vatnajökull ice cap, Iceland, *Geophys. Res. Lett.*, *19*(21), 2123–2126.

Sigmundsson, F., P. Einarsson, R. Bilham, and E. Sturkell (1995), Rift-transform kinematics in south Iceland: Deformation from Global Positioning System measurements, 1986 and 1992, *J. Geophys. Res.*, *100*, 6235–6248.

Sigmundsson, F., P. Einarsson, S. T. Rögnvaldsson, G. R. Foulger, K. M. Hodgkinsson, and G. Thorbergsson (1997), The 1994–1995 seismicity and deformation at the Hengill triple junction, Iceland: Triggering of earthquakes by minor magma injection in a zone of horizontal shear stress, *J. Geophys. Res.*, *102*, 15,151–15,161.

Stefánsson, R., and P. Halldórsson (1988), Strain release and strain build-up in the south Iceland seismic zone, *Tectonophysics*, *152*, 267–276.

Stefánsson, R., R. Bödvarsson, R. Slunga, P. Einarsson, S. Jakobsdóttir, H. Bungum, S. Gregersen, J. Havskov, J. Hjelme, and H. Korhonen (1993), Earthquake prediction research in the South Iceland Seismic Zone and the SIL project, *Bull. Seismol. Soc. Am.*, *83*, 696–716.

Stefánsson, R., G. Gudmundsson, and P. Halldórsson (2003), The South Iceland earthquakes 2000—A challenge for earthquake prediction research, *Rep. VI-R03017*, 21 pp., Icelandic Meteorol. Off., Reykjavík.

Tryggvason, A., S. T. Rögnvaldsson, and Ó. G. Flóvenz (2002), Three dimensional imaging of the P- and S-wave velocity structure and earthquake locations beneath southwest Iceland, *Geophys. J. Int.*, *151*, 848–866.

Wessel, P., and W. H. F. Smith (1998), New, improved version of generic mapping tools released, *Eos Trans. AGU*, *79*(47), 579.

Yuen, D. A., R. Sabadini, P. Gasperini, and E. Boschi (1986), On transient rheology and glacial isostasy, *J. Geophys. Res.*, *91*, 11,420–11,438.

T. Árnadóttir, Nordic Volcanological Center, Institute of Earth Sciences, Askja, Natural Sciences Building, Sturlugata 7, IS-101 Reykjavík, Iceland. (thora1@hi.is)

K. L. Feigl, Department of Terrestrial and Planetary Dynamics, Centre National de Recherche Scientifique, 14 ave. E. Belin, 31400 Toulouse, France. (feigl@dtp.obs-mip.fr)

W. Jiang, GPS Research Center, Wuhan University 129 Luoyu Road, Wuhan 430079, China. (wpjiang@whu.edu.cn)

S. Jónsson, Institute of Geophysics, ETH Hoenggerberg, CH-8093 Zurich, Switzerland. (sj@erdw.ethz.ch)

F. F. Pollitz, U.S. Geological Survey, 345 Middlefield Road, MS 977, Menlo Park, CA 94025, USA. (fpollitz@usgs.gov)